Chemical Engineering Journal 430 (2022) 132766

Contents lists available at ScienceDirect

Chemical Engineering Journal

journal homepage: www.elsevier.com/locate/cej

Photocatalytic oxidation mechanism of Gas-Phase VOCs: Unveiling the role of holes, •OH and $•O_2^-$

Zepeng Rao [a,b], Guanhong Lu [a], Lu Chen [a], Asad Mahmood [a], Gansheng Shi [a], Zixia Tang [a], Xiaofeng Xie [a,*], Jing Sun [a,*]

[a] State Key Lab of High Performance Ceramics and Superfine Microstructure, Shanghai Institute of Ceramics, Chinese Academy of Sciences, 1295 Dingxi Road, Shanghai 200050, China

[b] University of Chinese Academy of Sciences, 19 (A) Yuquan Road, Beijing 100049, China

ARTICLE INFO

Keywords:
Photocatalytic oxidation
VOCs decomposition
ROS
Reaction pathways

ABSTRACT

To identify the distinctive role of reactive oxygen species (ROS) and trace the intermediates not only help to decompose the pollutants in high efficiency but also for avoiding more harmful intermediates formed. Here, we developed a new method to generate different ROSs by controlling the atmosphere to distinguish their role in the degradation of flowing gas-phase VOCs, including *o*-xylene, styrene, and acetaldehyde. This method is in good agreement with the traditional sacrificial agent capture experiment. The results show that •OH radicals play a dominant role in the degradation of *o*-xylene and styrene, while $•O_2^-$ radicals primarily take part in the acetaldehyde degradation. Additionally, we distinguish the role of holes, •OH and $•O_2^-$ played during the VOCs photo-oxidation through the radical trapping, *in situ* DRIFTS, and GC-MS analysis. Under the attack of $•O_2^-$ radicals, aromatic VOCs were photo-oxidized to intermediates containing benzene rings and ketones (i.e., toluene and butanone), while carbon chain compounds (i.e., 3-methylfuran and ethanol) tend to form under the action of •OH and holes. This can be associated with the different reaction paths initiated by ROS. For acetaldehyde removal, $•O_2^-$ species facilitate the formation of acids (i.e., acetic acid) while the •OH species and holes lead to the production of ketones (i.e., acetone). This work provides deep understanding on the role of various ROS in the photocatalytic oxidation of VOCs, which can guide the design of efficient photocatalysts, selective formation of intermediates to be easily decomposed or as raw materials for further application.

1. Introduction

Volatile organic compounds (VOCs) are constantly increasing in the atmosphere through many sources, such as various industrial operations, volatilization of plastic and paints products, and dismantling of electronic wastes, etc. [1,2]. The accumulation of VOCs in the atmosphere can cause serious health issues in humans and also aggravate environmental pollution problems, e.g., respiratory problems, liver, kidney, and skin diseases, depletion of ozone and formation of photochemical smog [3,4]. Therefore, it is important to prioritize the elimination of VOCs to protect our health and environment. In this regard, quite a few technologies have been developed for the VOCs abatement, such as absorption, thermal decomposition, and photocatalytic oxidation (PCO) [5]. Among these, PCO is regarded as a promising technology to eliminate VOCs due to low energy consumption and relatively simple operating conditions [5,6]. TiO_2 is one of the most studied materials for its potential use in the PCO technology due to its high oxidizing property, chemical stability and availability [7].

Currently, most endeavor in the VOCs abatement regime mainly focus on how to enhance VOCs elimination rate and mineralization efficiency of TiO_2 by element doping, morphology control, surface modification through co-catalysts and compositing with other semiconductor materials [8–15]. Their primary purpose is to completely mineralize VOCs into carbon dioxide and water. Additionally, fewer researchers roughly highlight the role of free radicals in the photodegradation of organic pollutants, for example, organic dyes' degradation in wastewater and gaseous VOCs [16–19]. Ding et al suggested that $•O_2^-$ radicals are the main active species in liquid-phase rhodamine B (RhB) photodegradation. Also, the $•O_2^-$ radicals were observed to significantly affect the methyl orange (MO) degradation [20,21]. However, these attempts did not disclose the role of ROS played deeply, instead, only ascribed the superior performance of $•O_2^-$ radicals to their

* Corresponding authors.
E-mail addresses: xxfshcn@163.com (X. Xie), jingsun@mail.sic.ac.cn (J. Sun).

https://doi.org/10.1016/j.cej.2021.132766
Received 28 June 2021; Received in revised form 30 August 2021; Accepted 28 September 2021
Available online 5 October 2021

higher ESR signals than that of •OH radicals. Similarly, •OH radicals were concluded as the dominate in the photodegradation of methyl blue (MB) compared to $\bullet O_2^-$ [22]. Liu et al. [23] reported that the photoinduced holes (h^+) play a leading role during the photocatalytic degradation of phenol, which could be associated with the strong oxidation power of holes. Also, •OH radicals have been primarily accounted for the toluene photodegradation while $\bullet O_2^-$ radicals and photoinduced h^+ were accounted crucially in benzene degradation [24,25].

However, the role of different ROS species played in VOCs decomposing and the formation of intermediates has not been systematically investigated. Moreover, what kind of degradation pathway can be deduced depending on the specified ROS or photogenerated holes have not been studied in detail. This situation is limited by two associated problems. 1) The underlying mechanism that the target VOCs are directly converted to other species or mineralized into CO_2 and H_2O is not clear. 2) The role of ROS is only distinctive through radicals' scavengers, which can only provide an overall performance of a particular type of radicals. Also, the introduction of radicals' scavengers (i.e., liquid-phase capture experiments) will change the original surface state of the catalyst, which cannot inherently reflect the nature of the gas–solid phase photocatalytic reaction. However, the gas–solid reactions are quite tricky, which involve multiple steps. For example, the initial adsorption of pollutant molecules is critical in the gas–solid photocatalysis. The absorptivity and degradation of these molecules are significantly affected by the molecular structure of pollutants, surface features of catalysts (i.e., surface atomic arrangement and coordination), as well as experimental conditions (i.e., flow rate, relative humidity, light intensity, and temperature). We have recently observed that the changes in surface states could significantly affect the absorptivity and subsequent reaction pathways [26]. Therefore, it is essential to develop a new method to capture free radicals in gas-phase and differentiate the role of ROSs played in VOCs degradation. We believe the above strategy will be powerful to, 1) enable us to understand the underlying degradation mechanism, 2) improve the selective conversion of VOCs, and 3) once the distinctive role of ROS is identified, the pollutant molecules can be converted to useful intermediate products for numerous industrial applications via controllable pathways. For example, acetophenone, converted from degradation of the target VOCs such as *o*-xylene and styrene, is an intermediate in organic chemical synthesis, plasticizers for plastics, solvents for fiber resins, and food flavors. At present, the synthesis methods of acetophenone mainly include ethylbenzene oxidation, acylation of benzene with acetic anhydride, benzene and acetyl chlorination, etc. Also, acetophenone is usually prepared by air oxidation of ethylbenzene in the industry.

Herein, *o*-xylene, styrene and acetaldehyde were used as typical VOCs to investigate the role of photoinduced holes, •OH and $\bullet O_2^-$ during the process of photodegradation. We propose a new strategy (gas-phase capture test) to comprehend the role of ROS during the different VOCs elimination. Additionally, *in situ* Diffuse Reflectance Infrared Fourier Transform Spectroscopy (DRIFTS) and Gas Chromatography-Mass Spectrometer (GC-MS) were used to discriminate the intermediates and deduce the degradation pathways of VOCs with different free radicals. Finally, a detailed mechanism is proposed, which specify the effect of holes, •OH and $\bullet O_2^-$ took part in photocatalytic oxidation. This work provides deeper understanding on TiO_2 photocatalyst towards the VOCs degradation under different atmosphere condition and lays a foundation for realizing the selective conversion of VOCs.

2. Experimental

2.1. Materials

Anatase TiO_2 powders (AT0), sodium oxalate ($Na_2C_2O_4$), *tert*-butanol (TBA) and p-benzoquinone (PBQ) were produced by Sigma–Aldrich. Potassium dichromate ($K_2Cr_2O_7$) was received from Aladdin Industrial Co. 5,5-dimethyl-1-pyrroline N-oxide (DMPO) was purchased from Sigma Chemical Co. All chemicals were used as received without any further purification except for anatase. The initial anatase powders (AT0) were heat treated at 350 °C for 30 min and labeled AT.

2.2. Characterization

Fourier transform infrared (FTIR, iN10, Thermo Fisher), scanning electron microscope (SEM, Magellan 400, FEI), high resolution transmission electron microscope (HRTEM, JEM-2100, JEOL), X-ray diffraction (XRD, D8 ADVACE, Bruker), UV–vis Diffuse reflectance spectroscope (DRS) (Lambda 950, Perkin–Elmer), Raman spectra (DXR, Thermo Fisher), photoluminescence (PL, LS55, Perkin–Elmer) and electron spin resonance (ESR, JES-FA200, Thermo Fisher) analysis were conducted to investigate the morphological, structural, optical properties and free radical production of anatase photocatalyst before and after heat treatment, respectively. *In situ* DRIFTS (IRTracer-100, Thermo Fisher) and GC-MS (TSQ 8000 Evo, Thermo Fisher) results were employed to analyze the formed intermediates and reaction pathways during the photocatalytic reaction of the target VOCs, respectively.

2.3. Photocatalytic properties of anatase towards VOCs

The adsorption and photodegradation properties of acetaldehyde, *o*-xylene and styrene were conducted using an automated flow reaction chamber (Fig. 1). The adsorption of the target VOCs on the as-prepared photocatalysts was studied through the dynamic adsorption analysis in the dark. Initially, anatase powders (150 mg) were dispersed in 1.5 mL of ethanol and sonicated for 3 h. Next, the mixed solution was uniformly applied on a glass substrate (16 × 13 cm^2) and air-dried. Finally, the samples were put into the photocatalytic reaction chamber. All of the adsorption and degradation experiments were performed in the presence of air, N_2, O_2, "$N_2 + H_2O$" and "$N_2 + O_2 + H_2O$", respectively. Among them, photocatalytic properties of anatase TiO_2 under "$N_2 + O_2 + H_2O$" condition was used as a reference sample to estimate the photocatalytic performance in air. In a typical procedure, we mixed one of the target VOC (*o*-xylene, styrene and acetaldehyde) from one cylinder while another gas (air, N_2, O_2, "$N_2 + H_2O$", and "$N_2 + O_2 + H_2O$") was flown through another cylinder. Both of these flowing gases, i.e., air and one VOC were mixed before being introduced into the reaction cell. The concentration of these gases was automatically controlled via a computer. For example, the initial concentration of *o*-xylene and styrene is 50 ppm flowing through the automated flow system with a flow rate of 40 sccm. The compressed air is allowed to flow using the same flow rate. In this way, the final concentration of the o-xylene and styrene is regarded as 25 ppm. The final concentration of acetaldehyde is 500 ppm when the original concentration of acetaldehyde is 1000 ppm under similar circumstance. Notably, before the photocatalytic tests (including photocatalytic properties and *in situ* DRIFTS analysis), each sample was put into vacuum oven to dry for 12 h, which make sure that the $\bullet O_2^-$ or •OH radicals were not formed. The photocatalytic activity was evaluated by the removal ratio of gas-phase VOCs. The removal efficiency (RE) of VOC was determined as $RE = (C_0 - C)/C_0 \times 100\%$, where C_0 and C (ppm) are initial and real-time concentration of VOC, respectively. The mineralization efficiency (ME - selectivity of CO_2) of VOC was calculated by the formula: $ME(\%) = [(CO_{2out})\text{-}(CO_{2in})]/[Nvoc \times (C_{in}) \times RE(\%)] \times 10000$, where CO_{2out} and CO_{2in} are the outlet and inlet concentrations of CO_2. N*voc* represents the number of C atoms for the target VOCs ($N_{acetaldehyde} = 2$, $N_{o\text{-}xylene} = 8$ and $N_{styrene} = 8$). C_{in} and RE(%) are the inlet concentration and removal efficiency of gaseous VOCs, respectively.

2.4. ROS quenching experiments

Gas-phase capture experiments: We used three different carrier gases, which can facilitate the selective formation of different ROSs. In

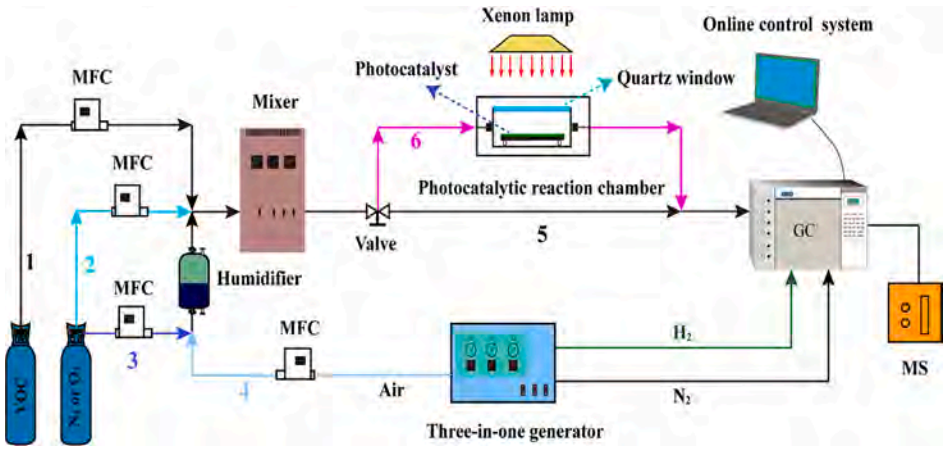

Fig. 1. Measurement setup for photocatalytic removal gas-phase VOCs with real-time monitoring and testing.

this way, their role can be assessed. For example, when N_2 was used as a carrier gas with target VOCs, according to formula (1)-(3), after light irradiation, only photogenerated electrons (e^-) and holes (h^+) were produced and •OH and $•O_2^-$ will not be formed. Thus, the role of photogenerated h^+ can be determined under N_2 carrier gas due to the weak oxidizing ability of photogenerated e^- in the gas–solid photoreactions [24]. Similarly, when the tests were performed in the presence of O_2, $•O_2^-$ and h^+ were formed ($•O_2^- > h^+$). Combined with the results under N_2 conditions (h^+), which can further highlight the effect of the $•O_2^-$ radicals during the VOCs degradation. When the experiments were conducted under the existence of "N_2 + H_2O", the •OH radicals were produced, hence, the role of •OH radicals can be examined in detail. This is because the photogenerated h^+ under "N_2 + H_2O" will react quickly with H_2O to form •OH (i.e., photogenerated h^+ is continuously consumed). Thus, the number of •OH species would be much higher than that of h^+, therefore, the catalytic properties under "N_2 + H_2O" condition can be principally attributed to the •OH radicals. In this way, the formation of a particular radical can be controlled to isolate its role during the VOCs removal.

$$Photocatalyst + hv \rightarrow h^+ + e^- \quad (1)$$

$$e^- + O_2 \rightarrow \bullet O_2^- \quad (2)$$

$$h^+ + H_2O \rightarrow H + \bullet OH \quad (3)$$

Liquid-phase capture experiments: To measure the feasibility of the gas-phase capture experiment results and confirm the role of free radical in photodegradation efficiency, liquid-phase capture experiments were carried out. The scavenger solutions used for quenching of electron, hole, $•O_2$ and •OH were $K_2Cr_2O_7$, $Na_2C_2O_4$, p-benzoquinone (PBQ) and *tert*-butanol (TBA), respectively [24,25]. Initially, 200 mg of sacrificial agent was dissolved in water or ethanol, and then 100 mg of catalyst was dispersed in the obtained solution. Finally, the suspension was ball milled for 8 h and then uniformly spin-coated on the glass sheet to perform the photocatalytic properties.

2.5. Detection of intermediates

In situ DRIFTS spectra: To better understand the photocatalytic reaction mechanisms, the adsorbed products on AT catalyst were analyzed by diffuse reflectance infrared Fourier transform spectroscopy (DRIFTS). Initially, about 32 mg of the AT powders were placed in the reaction cell. Next, the sample was heated from ambient temperature to 300 °C for 30 min under high-purity N_2 flux (flow rate 50 mL min^{-1}) to purge the catalyst. The background spectrum was collected after cooling down to room temperature. Subsequently, the target VOC and gas were introduced into the sample holder. Once, the adsorption was carried out for 90 min to achieve the adsorption–desorption equilibrium in the dark, the sample was irradiated using the xenon lamp (CHF-XM-250 W). The *in-situ* DRIFTS data were automatically recorded using a software with a constant time step of 15 min.

GC-MS analysis: All of the GC-MS results were obtained under the gas-phase capture experiments. Headspace method was used to directly detect the absorbed intermediates. In a typical procedure, the sample powders (150 mg) after the photocatalytic degradation of 4 h was transferred into a 100 mL of opaque bottle to avoid further photocatalytic reactions. The samples were subsequently subjected to GC-MS tests. The temperature of the column was raised from 35 °C to 100 °C with a step size of 10 °C min^{-1} while keeping the dwell time of 1 min at this temperature, which was further increased to 200 °C at 15 °C min^{-1} maintaining for 3 min and rose to 280 °C at 20 °C min^{-1} holding for 1 min. Mass spectra were recorded in electron ionization mode at 250 °C of an ion source under the full scan mode (*m/z* 50–400).

3. Results and discussion

3.1. Morphology, optical and structural properties of photocatalysts

Generally, the commercial anatase powders, might be contaminated (carbonaceous residues) during processing and packaging (Fig. S1a). This can affect the adsorption behavior of VOCs, thereby influencing the photocatalytic reaction routes, which was confirmed by *in situ* DRIFTS spectra (Fig. S2). The obvious difference of VOCs adsorption and photodegradation were observed in AT0 and AT samples. This could be associated with the presence of carbonaceous residues in AT0. To overcome this effect, the initial sample (AT0) was heat treated. As shown in Fig. S1a, the organic functional groups in the range of 3300–1300 cm^{-1} were eliminated by heat treatment. It is noteworthy that the agglomeration or particle size of AT was observed to increase slightly compared with AT0 sample (Fig.S1b). Due to this processing temperature, enhanced intensity could be observed on the peak profiles in XRD (Fig. S3c) and Raman spectra (Fig. S3d), which can be attributed to the improved crystallinity after heat treatment at 350 °C for 0.5 h. No significant changes were observed in the UV–vis (Fig. S3a) and PL spectra (Fig. S3b) and ESR data for active species (Fig. S4). After being thermal treatment at 350 °C, the surface carbonaceous residues on anatase were removed without altering the inherent structure.

3.2. The effect of active species during different VOCs photodegradation

Photocatalytic activity of the sample to degrade *o*-xylene and the role of active species played were evaluated under five different atmospheric conditions as shown in Fig. 2. It is worth noting that the photodegradation trends of *o*-xylene under the presence of "N_2 + H_2O + O_2"

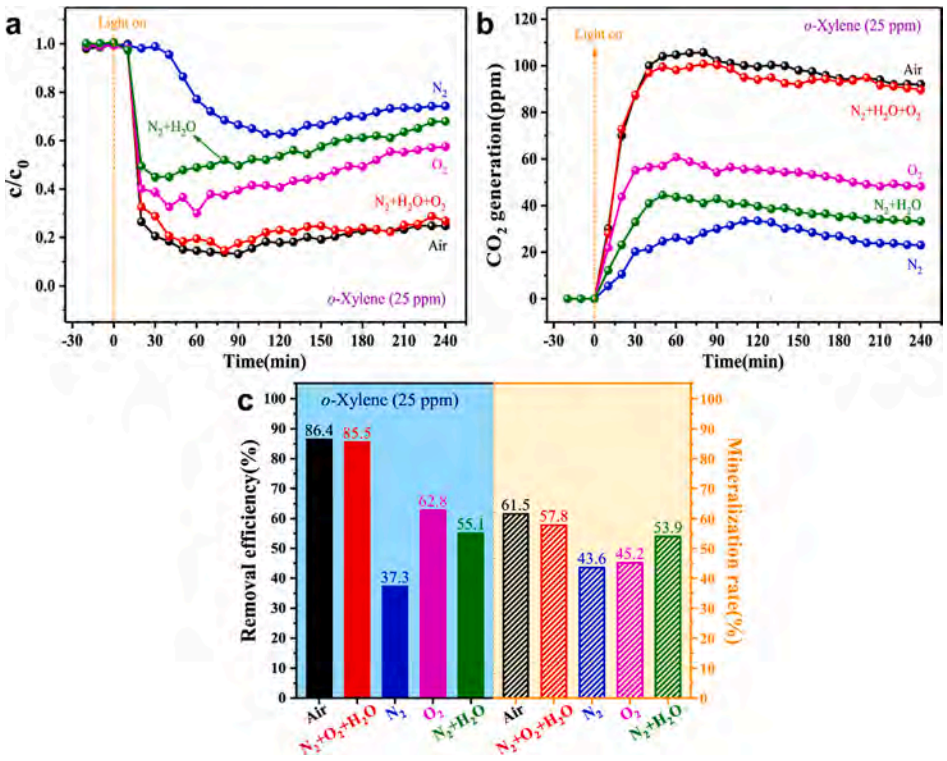

Fig. 2. (a) Degradation curves, (b) mineralization curves and (c) the corresponding removal efficiency and mineralization rate of *o*-xylene on AT under different atmospheric conditions.

was much similar to that in air condition (Fig. 2). Thus, "$N_2 + H_2O + O_2$" mixture can be used to simulate the reaction occurred in air condition. The C/C_0 ratio decreased sharply at initial stage, gradually reached a platform and final start to increase with the processing of photocatalytic reaction (Fig. 2a). This is because the generation of byproducts occupied the active sites on the catalyst surface, and eventually leading to the deactivation (the C/C_0 ratio increased with time) of the catalyst. A detailed explanation was reported in our previous work [8]. For *o*-xylene degradation under different atmospheric gases, the removal (RE) and mineralization efficiency (ME) over the AT sample followed the order (Fig. 2c): air > O_2 > $N_2 + H_2O$ > N_2. The RE and ME of *o*-xylene over the catalyst were 62.8% and 45.2% under O_2 atmosphere (with main oxidants as $\bullet O_2^-$ and h^+), respectively. RE and ME were 37.3% and 43.6% respectively in N_2 (with main oxidant as photogenerated h^+). Notably, the ME under the two conditions (i.e., O_2 and N_2) was almost similar (43.6% for N_2 and 45.2% for O_2), which showed that the photocatalytic performance under O_2 atmosphere was mainly derived from photoinduced h^+. The photocatalytic performance under "N_2 + H_2O" (with main oxidant as •OH) condition (RE is 55.1% and ME is 53.9%) was higher than that in N_2 atmosphere (with main oxidant as h^+) (RE is 37.3% and ME is 43.6%), suggesting that the role of •OH was stronger than that of h^+ in the degradation process. Based on these results, it can be concluded that the order of ROS influence during the *o*-xylene photodegradation was: •OH > h^+ > $\bullet O_2^-$. Thus, the •OH radicals play a predominated role in the photocatalytic reaction of *o*-xylene. Liquid-phase capture tests further verified this phenomenon. As shown in Fig. S5c, RE of *o*-xylene was 22.6% and ME was 18.6% when the •OH radicals were captured by TBA. When $Na_2C_2O_4$ was used to capture h^+, RE and ME were 50.8% and 25.5%, respectively. RE of *o*-xylene was 65.7% and ME was 45.2% when the $\bullet O_2^-$ species were captured by PBQ. RE was 82.1% and ME was 58.3% when $K_2Cr_2O_7$ captured photogenerated e^-. Again, the order for the effect of ROS on *o*-xylene degradation was recorded as: •OH > h^+ > $\bullet O_2^-$. This further confirmed that •OH played a more important role than any other ROS during the photocatalytic reaction of *o*-xylene. The results of the gas-phase capture experiment were similar to those of the traditional liquid-phase capture experiment, indicating that the developed gas-phase capture method in this work was effective and feasible. Additionally, a similar result was observed during the photocatalytic removal of gaseous styrene (Fig. S6), the result confirmed the dominant role of •OH radicals during the styrene removal.

Interestingly, similar gas-phase capture results were observed during the degradation of *o*-xylene and acetaldehyde under the existence of different atmospheric gases (Figs. 2 and 3), i.e., air > O_2 > $N_2 + H_2O$ > N_2. However, in the case of acetaldehyde elimination, the highest RE and ME of acetaldehyde (69.5% and 80.1%) were achieved in the existence of O_2 (Fig. 3c), O_2 (69.5% and 80.1%) > $N_2 + H_2O$ (30.1% and 28.8%) > N_2 (12.7% and 23.5%), indicating that these photocatalytic activities could be ascribed to the effect of $\bullet O_2^-$ and h^+. Additionally, the RE and ME were respectively 12.7% and 28.5% under N_2 existence (or h^+), which showed that the contribution of h^+ in the degradation of acetaldehyde was minimal. The excellent photocatalytic performance under O_2 was mainly derived from the contribution of $\bullet O_2^-$. Similarly, when the test was conducted in the presence of "$N_2 + H_2O$" (generating •OH), the lower RE (30.1%) and ME (28.8%) of acetaldehyde suggested that •OH has little effect on the degradation activity. The order for the effect of ROS on acetaldehyde degradation was recorded as: $\bullet O_2^-$ > •OH > h^+. The above results showed that $\bullet O_2^-$ played a more dominant role during the photoreaction of gas-phase acetaldehyde in contrast to any other ROS. This role was further evidenced by the liquid-phase capture analysis, where the order for MR and ME under the effect of different sacrificial agents were as follows (Fig. S7c): PBQ (28.7% and 18.2%) > TBA (61.2% and 79.3%) > $Na_2C_2O_4$ (75.9% and 77.2%) > $K_2Cr_2O_7$ (81.3% and 74.7%). This showed that the photocatalytic activity was the weakest when PBQ captured the $\bullet O_2^-$, further confirming the dominant effect of $\bullet O_2^-$ radicals on the degradation of acetaldehyde.

According to the above results, during the photodegradation of o-xylene and styrene, the existence of •OH radicals ("$N_2 + H_2O$" condition) or the absence of •OH (captured by TBA) has the greatest impact on the photocatalytic performance of the catalyst. Due to the Lewis base

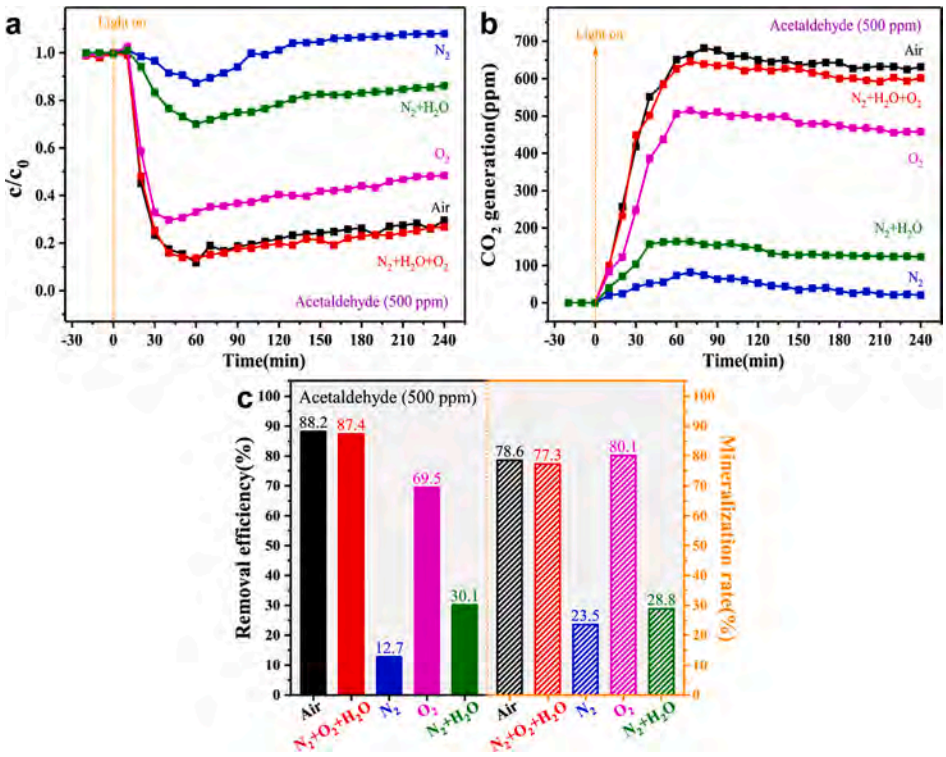

Fig. 3. (a) Degradation curves, (b) mineralization curves and (c) the corresponding removal efficiency and mineralization rate of acetaldehyde over AT under different atmospheric conditions.

properties (electron pair donor) of *o*-xylene or styrene molecules, electrons are easily transferred from the *o*-xylene or styrene molecules to the catalyst after adsorption and more •OH radicals formed [26]. Additionally, compared with the other active species, •OH has the higher oxidation ability to break the benzene ring of aromatic VOCs. So, the •OH radicals are the main active species in the degradation of these two aromatic VOCs. On the contrary, more $\bullet O_2^-$ species will be generated when acetaldehyde molecules, with the Lewis acid properties (electron pair acceptor), are adsorbed on TiO_2. Electrons were prone to be attracted by acetaldehyde molecules, more $\bullet O_2^-$ radicals were generated and played a key role in acetaldehyde degradation [26]. In this way, the different free radical formation under the electron gain or loss by the VOCs molecules will significantly affect the species of ROSs and finally influence the degradation process. Therefore, based on the above analysis, •OH was the main reactive radical in o-xylene and styrene photodegradation while $\bullet O_2^-$ played a leading role during the photocatalytic removal of acetaldehyde.

3.3. The specifical oxidation path of VOC controlled by different reactive species

To disclose the specific photocatalytic reaction routes of the three VOCs over AT sample under the influence of different ROS, *in situ* DRIFTS analysis was performed. As indicated in Fig. S8, no new bands were generated and no significant changes appeared in the normalized DRIFTS band's intensity over reference the ZrO_2 sample (the stable insulation material) during the VOCs adsorption and degradation. This showed that no photolysis happened during the target VOCs degradation. Noticeably, oxygen containing functional groups were observed in the presence of N_2 during the photodegradation of *o*-xylene. The oxygen containing species are anticipated to derive from the lattice oxygen (O_L) of AT sample, which participated in the photocatalytic reaction. This could be directly confirmed by the ESR signals of photocatalyst before and after photodegradation. As indicated in Fig. S9a, the concentration of oxygen vacancies increased after photoreaction with the gas-phase *o*-xylene for 4 h, indicating the loss of lattice oxygen. Similar results were appeared in the elimination of styrene and acetaldehyde (Fig. S9b and c). Thus, the intermediate species containing oxygen were produced during the three VOCs removal under the existence of N_2.

As displayed in Fig. 4 and Table S1, the characteristic bands at 3749, 3650 and 3637 cm^{-1} were assigned to the vibration mode of hydroxy groups ν(OH) in H_2O [27,28]. The sharp peaks located at 3564, 3545 and 3525 cm^{-1} corresponding to the ν(OH) vibration of benzyl alcohol and aliphatic alcohol [29–31]. The IR bands in the range from 3070 to 2870 cm^{-1} were associated with the vibration mode of methyl groups of aromatic compounds [32]. The typical peaks at 1732, 1716, 1699, 1681 and 1650 cm^{-1} were due to the carbonyl group (C = O) of aliphatic or aromatic ketone and the ν(H-C = O) vibration of aldehydes or aromatic aldehyde [33,34]. The 1600 cm^{-1} could be attributed to the benzene ring vibration [32,33]. Five IR bands at 1574, 1558, 1539, 1523, 1508 and 1489 cm^{-1} were attributed to the vibration modes of ν_{as}(COO) and ν_s(COO) for aliphatic or aromatic carboxylate [34,35]. The FTIR bands in the range of 1472–1377 cm^{-1} were ascribed to $\delta_{as}(CH_3)$ and $\delta_s(CH_3)$ vibration of aliphatic compounds [35,36]. The weak peaks at 1303–1288 cm^{-1} were due to ν(C-O) of aliphatic carboxylate [35,37]. Notably, some weak bands, centered at 3564, 1681, 1650 and 1558 cm^{-1} (aromatic byproducts), were observed in the process of dark adsorption, this indicated that chemisorption of *o*-xylene occurred on the catalyst surface. Similar behavior was observed in the previous works during the photodegradation of gas-phase toluene [32,34]. However, aliphatic substances (1288 cm^{-1}) appeared after light irradiation, suggesting the benzene rings were opened. Additionally, the DRIFTS absorbance intensities of the characteristic bands increased with increasing the illumination time. These results suggested that *o*-xylene molecules could be photodegraded into smaller molecules including aliphatic intermediates and even CO_2 under the effect of ROS. As shown in Fig. 4g-h, 1650 cm^{-1} intensity in Fig. 4h is higher than that in Fig. 4g and 4i, and the peak (3564 cm^{-1}) intensity in Fig. 4h increased with the increasing reaction time while that in Fig. 4g and 4i decreased with increasing light irradiation time. These observations demonstrated that

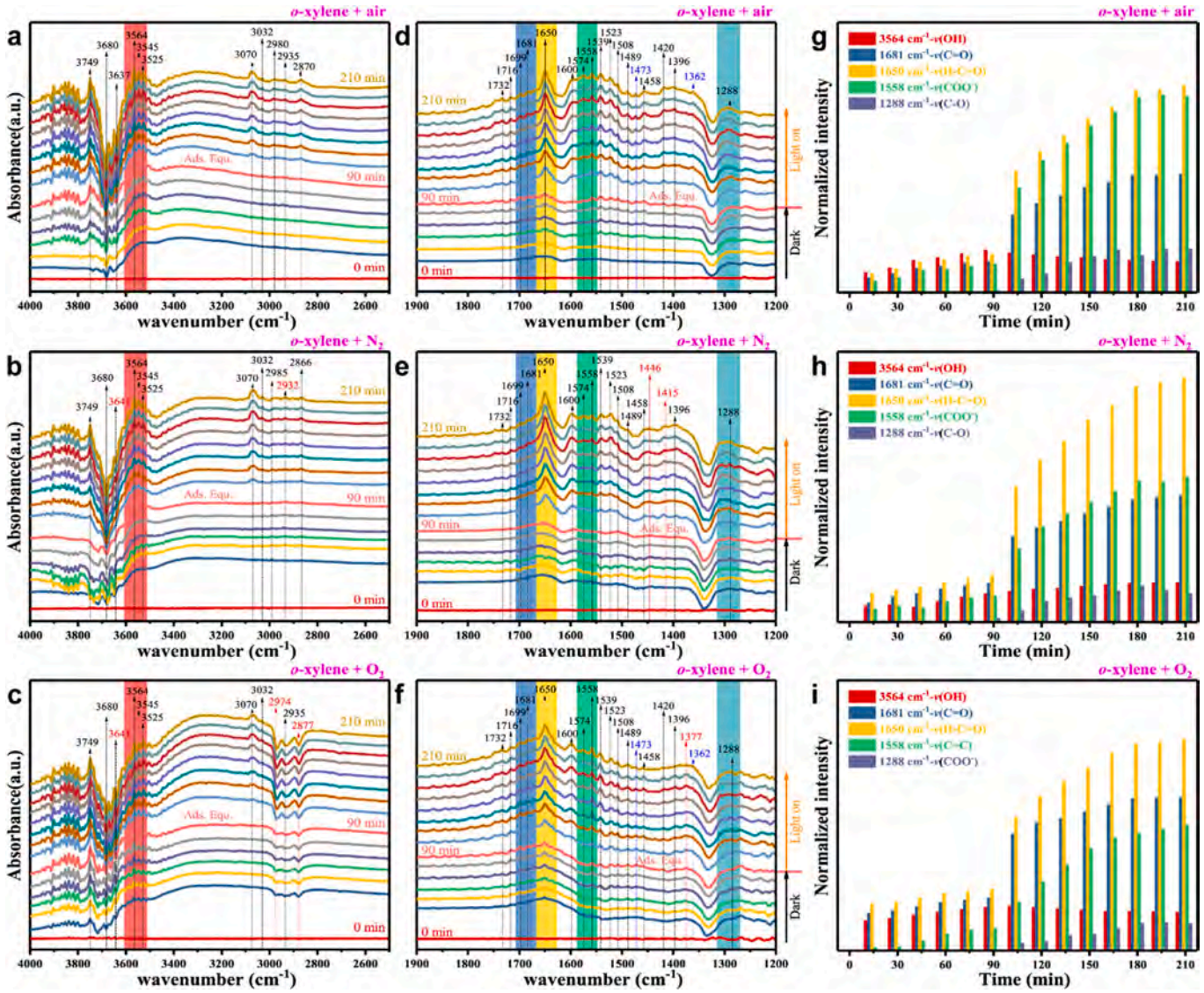

Fig. 4. *In situ* DRIFTS plots of gas-phase *o*-xylene over AT sample in the range of (a, b, c) 4000–2500 cm^{-1} and (d, e, f) 1900–1100 cm^{-1} under the presence of the different gases. The images (g, h, i) show the histogram of the corresponding organic functional groups after normalization. The same value of Y-axis for figures (a, b, c), (d, e, f) and (g, h, i), respectively.

the target VOCs could be converted to aldehydes and alcohols in the presence of holes and O_L. Moreover, it can be seen from Fig. 4i that the band at 1650 cm^{-1} (aldehydic group) is converted into 1681 cm^{-1} (C = O for ketones) under the influence of $\bullet O_2^-$ species. When the experiment is conducted under air condition (all free radicals), *o*-xylene can be easily degraded into carboxylate species (1558 cm^{-1} for $\nu(COO^-)$).

Meanwhile, similar *in situ* DRIFTS results were observed in the photocatalytic degradation of gaseous styrene (Fig. S10 and Table S2) and *o*-xylene (Fig. 4 and Table S1), which might be that the two target pollutants belong to aromatic VOCs. However, compared with *o*-xylene photoreaction, little difference was observed in the case of styrene degradation using *in situ* DRIFTS. For example, styrene molecules displayed easy conversion to aliphatic compounds including 1454 cm^{-1} for $\delta(CH_2)$ vibration of aliphatic acids and 1222 cm^{-1} for $r(CH_2)$ vibration of maleic anhydride [32,38,39]. This might be due to the different adsorption geometries on the sample surface of these two molecules and the differences in their own properties.

As indicated in Fig. 5 and Table S3, the chemisorption phenomenon happened in the case of acetaldehyde under the dark adsorption process. This is evidenced by new DRIFTS bands appeared in the range of 1173–4000 cm^{-1}without light irradiation. This behavior is somewhat similar to the previous work on acetaldehyde photodegradation by Hauchecorne et al. [35]. For illuminated sample, the peak absorbance at 1650 cm^{-1} (aldehydic group for acetaldehyde) obviously decreased with the increased irradiation time [40], indicating that the adsorbed VOC molecules are photodegraded into other products. Interestingly, the band intensity at 1620 cm^{-1} (C = C for crotonaldehyde) increased in dark adsorption while decreased after photoreaction [35,41], indicating that crotonaldehyde might be the main byproduct in dark adsorption process. The typical peaks at 1558 cm^{-1} for acids obviously increased with increasing reaction time under O_2 existence and a band intensity at 1173 cm^{-1} for ethers in the presence of O_2 was higher than that in other gases [35,42]. By combining with other experimental atmospheric conditions, the peak intensity at 1699 cm^{-1} (ketones) is the highest under N_2 conditions [33,35]. Therefore, it can be inferred that $\bullet O_2^-$ radicals facilitated the conversion of acetaldehyde into acids and ethers. Additionally, the existence of electrons and holes are beneficial for decomposing acetaldehyde into ketones.

Since, the organic functional groups in the FTIR spectra cannot be resolved efficiently due to numerous superimposed peaks and shoulder peaks, we further used the GC-MS analysis to further disclose the oxidation path of VOCs over the photocatalyst under the influence of

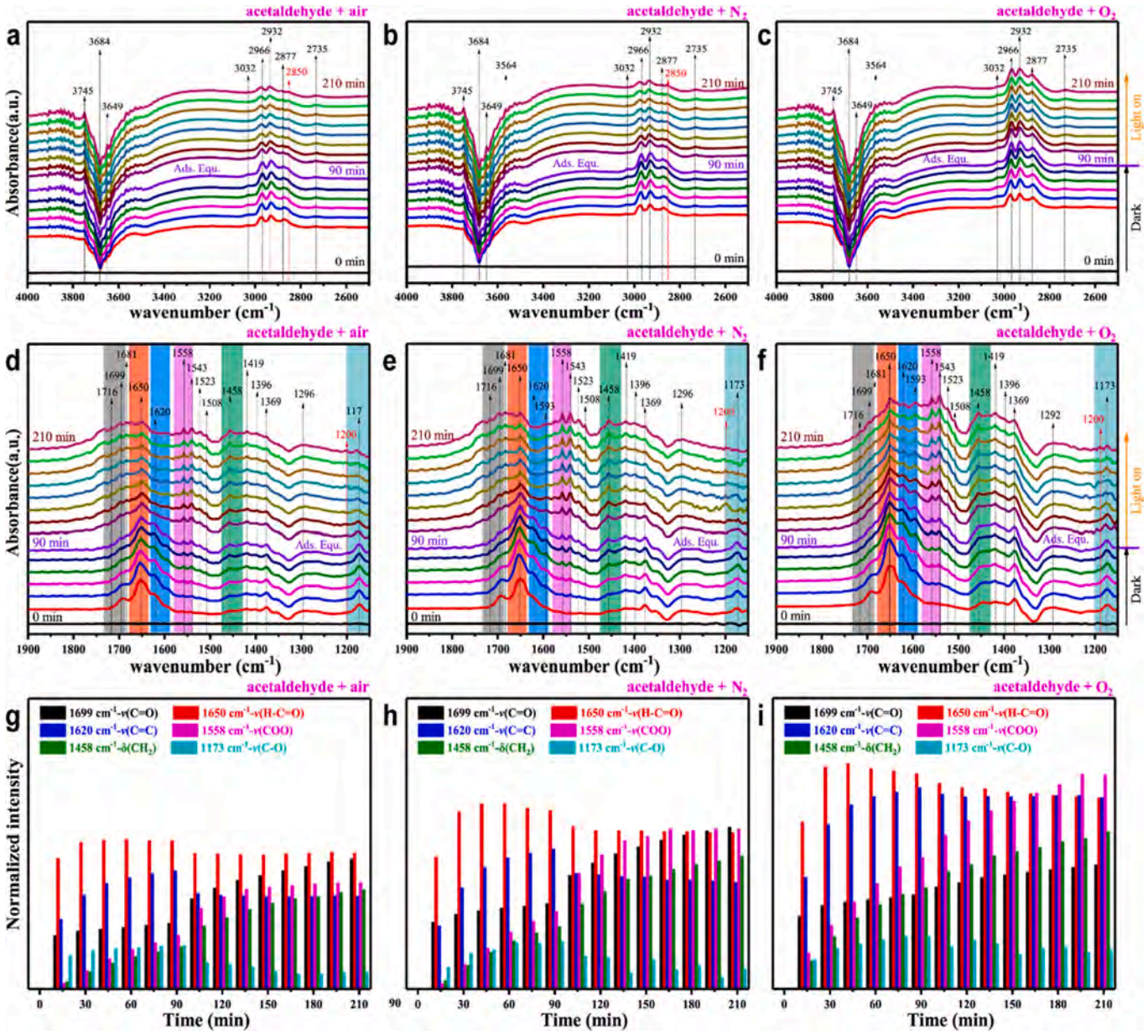

Fig. 5. *In situ* DRIFTS profiles of gaseous acetaldehyde on AT sample in the range of (a, b, c) 4000–2500 cm^{-1} and (d, e, f) 1900–1100 cm^{-1} under the existence the different free radicals. The images (g, h, i) show the histogram of the corresponding organic functional groups after normalization. The same value of Y-axis for figures (a, b, c), (d, e, f) and (g, h, i), respectively.

different gases (i.e., generating of different ROS) (Figs. 6 and 7, Fig. S11 and Table S4-S6). In any case, *o*-xylene intermediates analysis showed the existence of *o*-toluadehyde (Fig. 6 and Table S4). Interestingly, acetaldehyde, ethanol, acetone, 2,2-dimethyl-1,3-dihydroindene, *o*-methylacetophenone and α-methyl styrene were main intermediates in the *o*-xylene photoreaction when only N_2 (with main oxidant as holes) exist in the test system. Among them, most intermediate species with ring-opened indicated that the photogenerated h^+ are beneficial to the aromatic ring opening process. This was further evidenced by the GC-MS analysis, for the sample degraded under the influence of O_2 (or holes and $\bullet O_2^-$), where the open-ring intermediates including acetaldehyde, ethanol and acetone also appeared. But toluene, butanone, 2,2,4,6,6-pentamethylheptan detected under the O_2 (or h^+ and $\bullet O_2^-$) condition were higher than those observed in N_2 (or h^+) presence, suggesting that $\bullet O_2^-$ species mainly lead to the generation of these three intermediates. It is understandable why the GC-MS data obtained in "$N_2 + H_2O$" (or h^+ and •OH) are similar to that under N_2 presence, this was due to the fact that •OH species are converted from holes or they have similar oxidation capacity. However, there is a little different existing in GC-MS results under "$N_2 + H_2O$" (with main oxidants as h^+ and •OH) and N_2 (with main oxidant as h^+) condition, namely, •OH favor the production of 3-methylfuran. *o*-Xylene is easily degraded into *o*-tolualdehyde and acetaldehyde containing aldehyde group (CHO) over AT catalyst under the presence of all ROS.

Although similar radicals (•OH) played a leading role during the *o*-xylene and styrene photoreaction, the difference was observed in the formation of intermediates. As shown in Fig. S11 and Table S5, it was observed in N_2 (or h^+) capture system the photoinduced holes lead to the formation of acetophenone and ethanol. Similar trends were seen in the presence of •OH ("$N_2 + H_2O$" condition), whilst styrene was easily converted to benzene, toluene and benzaldehyde in the existence of $\bullet O_2^-$ (O_2 gases). The target pollutants tend to degrade into carbon chain containing species including acetone and butanone under all reactive species.

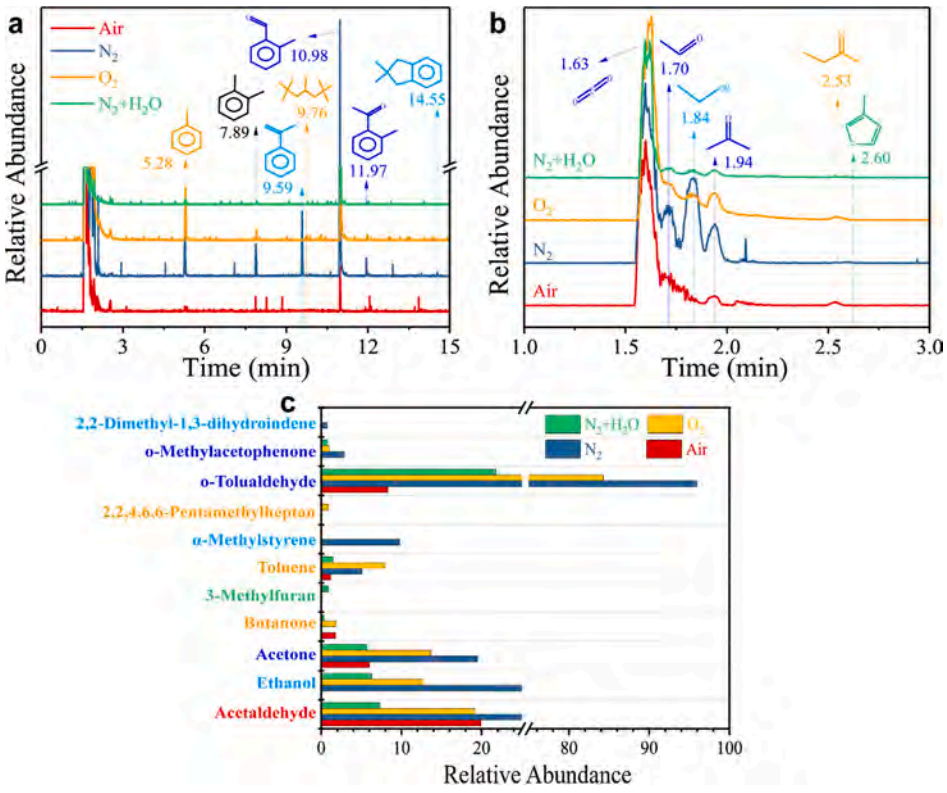

Fig. 6. GC-MS data of *o*-xylene photodegradation for 4 h over AT catalyst under the existence of different ROS, (a) the retention time from 0 to 15 min, (b) the enlarged spectra for retention time from 1 to 3 min and (c) the relative abundance of the corresponding intermediates.

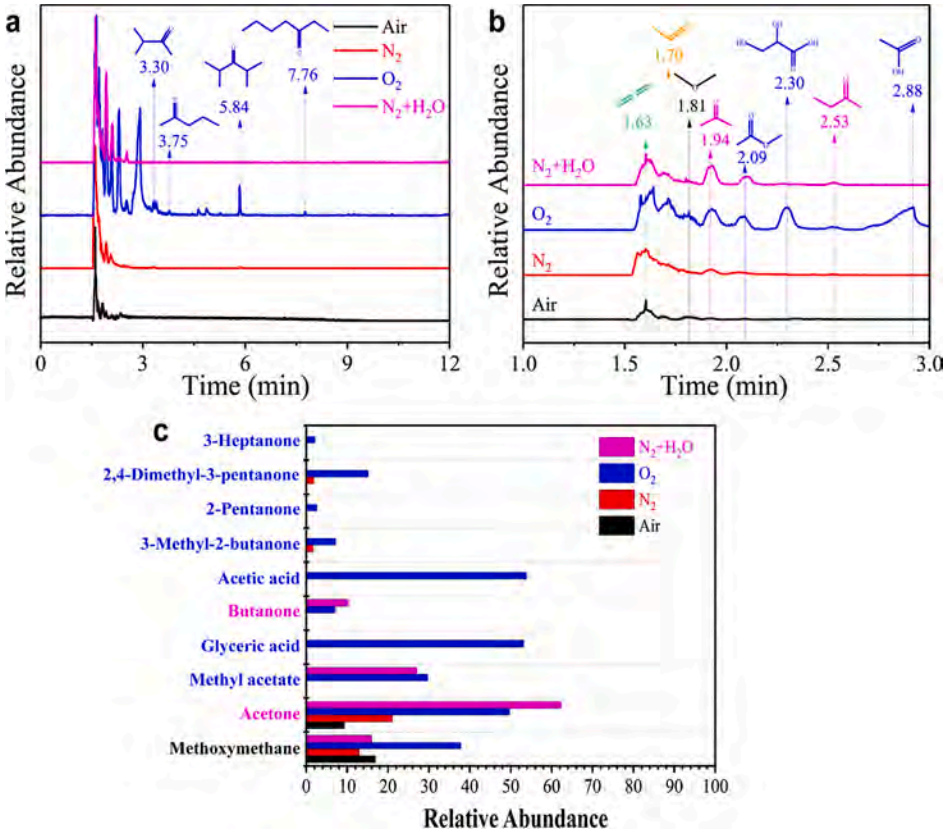

Fig. 7. GC-MS results of acetaldehyde photoreaction for 4 h on AT sample in the presence of different gases including air, N_2, O_2 and "$N_2 + H_2O$", (a) the retention time from 0 to 15 min, (b) the enlarged spectra for retention time from 1 to 3 min and (c) the relative abundance of the corresponding intermediates.

For acetaldehyde photoreaction (Fig. 7 and Table S6), the same byproducts, such as methoxymethane, acetone, 3-methyl-2-butanone and 2,4-dimethyl-3-pentanone, were detected over the AT surface under the N_2 (h^+ and e^-) and O_2 (h^+, e^- and $\bullet O_2^-$) gas-phase capture. The additional intermediates, including methyl acetate, glyceric acid, acetic acid, 2-pentanone, 3-heptanone, were found under the O_2 condition, which showed that these five species formed under the oxidization by $\bullet O_2^-$. Meanwhile, under the effect of holes and •OH ("$N_2 + H_2O$") and O_L, acetone and butanone were the main byproducts during acetaldehyde decomposition. In contrast to other systems, the minimum intermediates (only methoxymethane and acetone) were observed when all free radicals appeared in the test system.

The GC-MS results further confirm the *in-situ* DRIFTS observations. However, some possible intermediates appeared in the *in situ* FTIR were not observed in the GC-MS results, which could be associated with the detection limit and operation of GC-MS. Overall, combining DRIFTS results with GC-MS analysis, we can infer that the specific intermediates are generated under the role of different ROS during the photocatalytic degradation process of the three VOCs. As presented Fig. 8 and Fig. S12, the aromatic VOCs *o*-xylene and styrene are firstly decomposed by reactive radicals into compounds containing a benzene ring structure, and next oxidized to carbon chain containing intermediates, and eventually degraded into CO_2 and H_2O. For *o*-xylene molecules decomposition, the VOC is mainly converted into byproducts, including *o*-tolualdehyde and ethanol under the presence of h^+ and O_L. When the $\bullet O_2^-$ exists, pollutants tend to form toluene and butanone. While •OH species are beneficial to oxide *o*-xylene to ring-opening products 3-methylfuran. All ROS causes the conversion of target VOC into acetaldehyde. Similarly, ethanol is easily generated under the effect of h^+ and O_L during the process of gaseous styrene photodegradation. The $\bullet O_2^-$ radicals lead to the formation of benzaldehyde, toluene and benzene. The •OH species facilitate the aromatic ring opening process and all free radicals determine the final product as acetone.

Therefore, photoinduced h^+ and O_L played a key role in the generation of ethanol during *o*-xylene and styrene decomposition. The •OH dominates the opening of the aromatic ring, while $\bullet O_2^-$ species are not conducive to this process, but play a leading role in the production of ketones.

As shown in Fig. 9, acetaldehyde tends to decompose as acetone under the existence of h^+ and O_L. The $\bullet O_2^-$ radicals favor acids forming including acetic acid and glyceric acid while the •OH radicals facilitate ketones formation such as acetone and butanone. The target molecules are easily converted into methoxymethane under the effect of all ROS.

Notably, some intermediates, generated in the photocatalytic oxidation process of the three VOCs, are important biofuels, food additives and chemicals for various industrial applications. For example, acetophenone is an intermediate in organic chemical synthesis, plasticizers for plastics, solvents for fiber resins, and food flavors. Glyceric acid and its derivatives can promote ethanol catabolism, and its derived ester oligomers can resist trypsin activity. Additionally, glyceric acid can also be used as a food additive. Methoxymethane, a byproduct of acetaldehyde, can be used as an alkylating agent, foaming agent, refrigerant, solvent, extractant, anesthetic, fuel, civil composite ethanol, and a substitute for Freon aerosol. And it can also be used as various aerosol propellants in hair care, skin care, medicine, coatings, and its unique uses including dyes, fuel additives promoted abroad, pharmaceuticals, pesticide industries, etc. Thus, we can control the experimental conditions (different ROS) to produce desired byproducts, so as to "turn waste into treasure", which is of great significance for the environmental protection.

4. Conclusion

In summary, a new gas-phase capture method for investigating the role of ROS during the VOCs photodegradation was developed. Interestingly, different leading effects were observed in photoreaction of the investigated VOCs. The •OH radicals played a key role in *o*-xylene and styrene elimination while the $\bullet O_2^-$ species dominated the acetaldehyde degradation. Additionally, during the specific reaction process of VOCs molecules, including *o*-xylene and styrene, the •OH radicals facilitated the aromatic ring-opening and the mineralization of intermediates. Moreover, the photoinduced h^+ and O_L played a dominant role in the conversion of ethanol. While the $\bullet O_2^-$ radicals played a leading role in the formation of toluene and ketones (containing carbonyl groups). In the case of acetaldehyde removal, the $\bullet O_2^-$ radicals were regarded as crucial, which could facilitate the formation of acids while the •OH radicals dominated the production of ketones. This work provides a new insight into the photocatalytic decomposition of VOCs. It also provides a possible strategy for achieving the directional conversion of VOCs by controlling the experimental atmosphere, i.e., "turn waste into treasure" for several industrial applications.

Declaration of Competing Interest

The authors declare that they have no known competing financial interests or personal relationships that could have appeared to influence

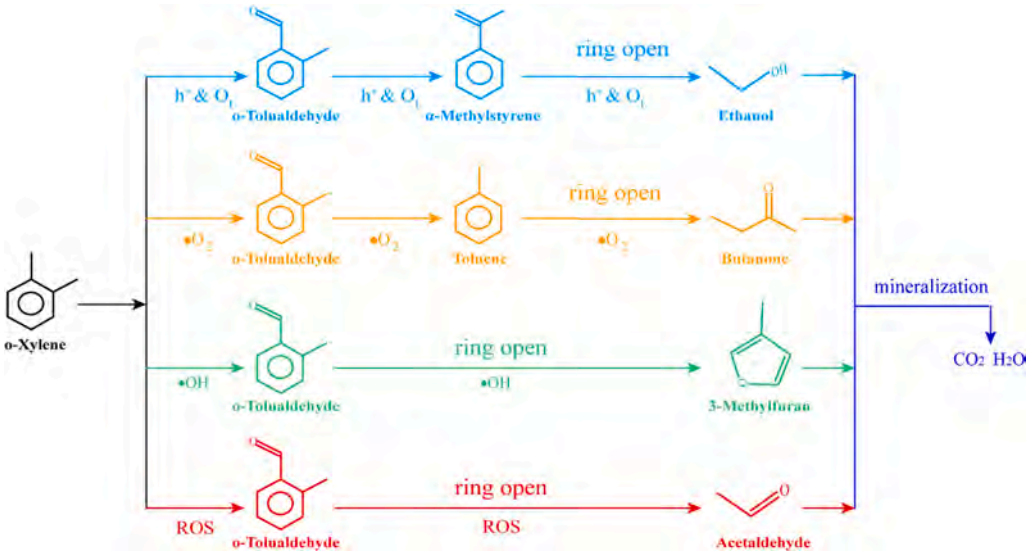

Fig. 8. Schematic diagram for the detailed role of different free radical species during the proposed photocatalytic reaction pathways of gaseous *o*-xylene.

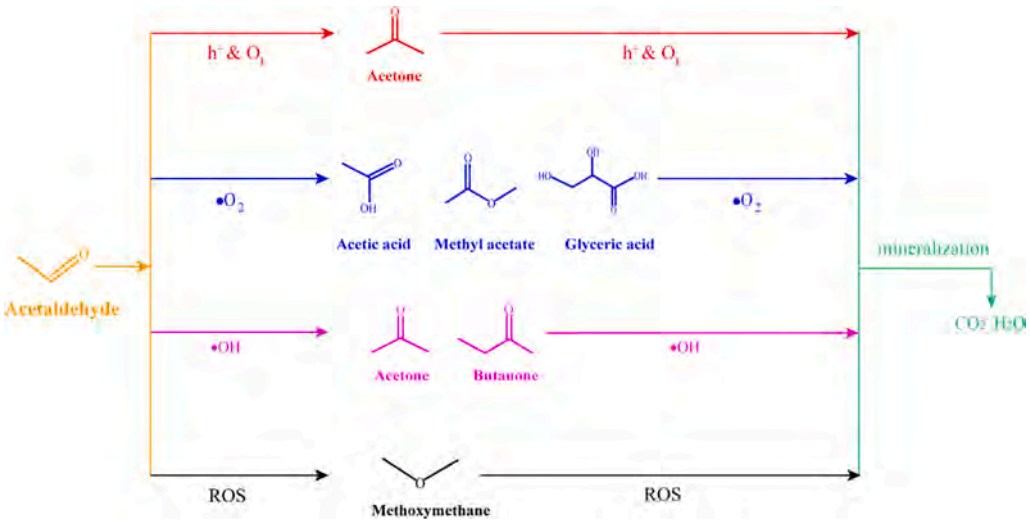

Fig. 9. Schematic diagram for the specific effect of different reactive species during the proposed photocatalytic oxidation routes towards gas-phase acetaldehyde.

the work reported in this paper.

Acknowledgment

This work was financially supported by the National Key Research and Development Program of China (2021YFE0110400, 2016YFA0203000), Shanghai Commission of Science and Technology Program (19DZ1202600, 20DZ1204100), the National Natural Science Foundation of China (Grant No. 41907303), the Innovation Fund of SICCAS (No. Y91ZC5150G).

Appendix A. Supplementary data

Supplementary data to this article can be found online at https://doi.org/10.1016/j.cej.2021.132766. *In situ* DRIFTS spectra of AT0 and AT samples at range of 4000–1000 cm^{-1}. UV–vis, PL, XRD, Raman data and ESR signals of DMPO- $\bullet O_2^-$ and DMPO- •OH adducts for AT0 and AT photocatalysts before and after heat treatment. The dynamic adsorption curves of anatase sample for flowing *o*-xylene, styrene and acetaldehyde. The mineralization plots of gas-phase capture and liquid-phase capture for different VOCs, the histogram of the corresponding mineralization efficiency. The photodegradation data of gas-phase capture and liquid-phase capture, and the mineralization plots of gas-phase capture and liquid-phase capture towards different VOCs. ESR signals of oxygen vacancies for AT sample before and after the photodegradation of gas-phase *o*-xylene, styrene and acetaldehyde for 4 h. *In situ* DRIFTS profiles of ZrO_2 for *o*-xylene, styrene and acetaldehyde from 4000 to 1000 cm^{-1}. *In situ* DRIFTS results of *o*-xylene on AT sample ranging from 4000 to 1000 cm^{-1} under the presence of air, O_2 and N_2 gas. GC-MS spectra of styrene photoreaction for 4 h on AT sample in the presence of different gases including air, N_2, O_2 and "N_2 + H_2O". The detailed role of ROS during the photocatalytic reaction path of gaseous styrene.

References

[1] J. Chen, Y. Huang, G. Li, T. An, Y. Hu, Y. Li, VOCs elimination and health risk reduction in e-waste dismantling workshop using integrated techniques of electrostatic precipitation with advanced oxidation technologies, J. Hazard. Mater. 302 (2016) 395–403.
[2] C. He, J. Cheng, X. Zhang, M. Douthwaite, S. Pattisson, Z. Hao, Recent advances in the catalytic oxidation of volatile organic compounds: a review based on pollutant sorts and sources, Chem. Rev. 119 (2019) 4471–4568.
[3] J.D. Spengler, K. Sexton, Indoor air pollution: a public health perspective, Science 221 (1983) 9–17.
[4] U. Pöschl, M. Shiraiwa, Multiphase Chemistry at the atmosphere–biosphere interface influencing climate and public health in the anthropocene, Chem. Rev. 115 (2015) 4440–4475.
[5] A.H. Mamaghani, F. Haghighat, C.S. Lee, Photocatalytic oxidation technology for indoor environment air purification: the state-of-the-art, Appl. Catal. B 203 (2017) 247–269.
[6] Y. Boyjoo, H. Sun, J. Liu, V.K. Pareek, S. Wang, A review on photocatalysis for air treatment: from catalyst development to reactor design, Chem. Eng. J. 310 (2017) 537–559.
[7] H. Chen, C.E. Nanayakkara, V.H. Grassian, Titanium dioxide photocatalysis in atmospheric chemistry, Chem. Rev. 112 (2012) 5919–5948.
[8] Z. Rao, G. Lu, A. Mahmood, X. Xie, J. Sun, Deactivation and activation mechanism of TiO_2 and rGO/Er^{3+}-TiO_2 during flowing gaseous VOCs photodegradation, Appl. Catal. B 284 (2021), 119813.
[9] Z. Rao, G. Shi, Z. Wang, A. Mahmood, X. Xie, J. Sun, Photocatalytic degradation of gaseous VOCs over Tm^{3+}-TiO_2: revealing the activity enhancement mechanism and different reaction paths, Chem. Eng. J. 395 (2020), 125078.
[10] Z. Rao, X. Xie, X. Wang, A. Mahmood, S. Tong, M. Ge, J. Sun, Defect chemistry of Er^{3+}-doped TiO_2 and its photocatalytic activity for the degradation of flowing gas-phase VOCs, The Journal of Physical Chemistry C 123 (2019) 12321–12334.
[11] Q. Zeng, X. Xie, X. Wang, Y. Wang, G. Lu, D.Y.H. Pui, J. Sun, Enhanced photocatalytic performance of Ag@TiO_2 for the gaseous acetaldehyde photodegradation under fluorescent lamp, Chem. Eng. J. 341 (2018) 83–92.
[12] A. Mahmood, G. Shi, Z. Wang, Z. Rao, W. Xiao, X. Xie, J. Sun, Carbon quantum dots-TiO_2 nanocomposite as an efficient photocatalyst for the photodegradation of aromatic ring-containing mixed VOCs: an experimental and DFT studies of adsorption and electronic structure of the interface, J. Hazard. Mater. 401 (2020), 123402.
[13] X. Dai, Y. Wang, X. Wang, S. Tong, X. Xie, Polarity on adsorption and photocatalytic performances of N-GR/TiO_2 towards gaseous acetaldehyde and ethylene, Appl. Surf. Sci. 485 (2019) 255–265.
[14] Q. Zeng, X. Wang, X. Xie, G. Lu, Y. Wang, S. Cheng Lee, J. Sun, TiO_2/TaS_2 with superior charge separation and adsorptive capacity to the photodegradation of gaseous acetaldehyde, Chem. Eng. J. 379 (2020), 122395.
[15] X. Dai, G. Lu, Y. Hu, X. Xie, X. Wang, J. Sun, Reversible redox behavior of Fe_2O_3/TiO_2 composites in the gaseous photodegradation process, Ceram. Int. 45 (2019) 13187–13192.
[16] K. Lv, B. Cheng, J. Yu, G. Liu, Fluorine ions-mediated morphology control of anatase TiO_2 with enhanced photocatalytic activity, PCCP 14 (2012) 5349–5362.
[17] J. Sun, X. Yan, K. Lv, S. Sun, K. Deng, D. Du, Photocatalytic degradation pathway for azo dye in TiO_2/UV/O_3 system: hydroxyl radical versus hole, J. Molecular Catal. A-Chem. 367 (2013) 31–37.
[18] K. Lv, X. Guo, X. Wu, Q. Li, W. Ho, M. Li, H. Ye, D. Du, Photocatalytic selective oxidation of phenol to produce dihydroxybenzenes in a TiO_2/UV system: hydroxyl radical versus hole, Appl. Catal. B-Environ. 199 (2016) 405–411.
[19] X. Li, X. Wu, S. Liu, Y. Li, J. Fan, K. Lv, Effects of fluorine on photocatalysis, Chin. J. Catal. 41 (2020) 1451–1467.
[20] P. Ding, J. Di, X. Chen, J. Zhao, K. Gu, Y.i. Zhang, S. Yin, G. Liu, J. Xia, H. Li, Partially etched $Bi_2O_2CO_3$ by metal chloride for enhanced reactive oxygen species generation: A tale of two strategies, Appl. Catal. B 245 (2019) 325–333.
[21] Z. Lu, L. Zeng, W. Song, Z. Qin, D. Zeng, C. Xie, In situ synthesis of C-TiO_2/g-C_3N_4 heterojunction nanocomposite as highly visible light active photocatalyst originated from effective interfacial charge transfer, Appl. Catal. B 202 (2017) 489–499.
[22] Y. Lv, Y. Zhu, Y. Zhu, Enhanced photocatalytic performance for the $BiPO_{4-x}$ nanorod induced by surface oxygen vacancy, The J. Physical Chem. C 117 (2013) 18520–18528.
[23] Y. Liu, W. Yao, D. Liu, R. Zong, M. Zhang, X. Ma, Y. Zhu, Enhancement of visible light mineralization ability and photocatalytic activity of $BiPO_4$/BiOI, Appl. Catal. B 163 (2015) 547–553.

[24] M. Sun, X. Wang, Z. Chen, M. Murugananthan, Y. Chen, Y. Zhang, Stabilized oxygen vacancies over heterojunction for highly efficient and exceptionally durable VOCs photocatalytic degradation, Appl. Catal. B 273 (2020) 119061, https://doi.org/10.1016/j.apcatb.2020.119061.
[25] X. Zheng, J. Wang, J. Liu, Z. Wang, S. Chen, X. Fu, Photocatalytic degradation of benzene over different morphology $BiPO_4$: Revealing the significant contribution of high–energy facets and oxygen vacancies, Appl. Catal. B 243 (2019) 780–789.
[26] Q. Zeng, X. Wang, X. Xie, A. Mahmood, G. Lu, Y. Wang, J. Sun, Band bending of TiO_2 induced by o-xylene and acetaldehyde adsorption and its effect on the generation of active radicals, J. Colloid Interface Sci. 572 (2020) 374–383.
[27] G. Martra, S. Coluccia, L. Marchese, V. Augugliaro, V. Loddo, L. Palmisano, M. Schiavello, The role of H_2O in the photocatalytic oxidation of toluene in vapour phase on anatase TiO_2 catalyst a FTIR study, Catal. Today 53 (4) (1999) 695–702.
[28] A.J. Maira, J.M. Coronado, V. Augugliaro, K.L. Yeung, J.C. Conesa, J. Soria, Fourier transform infrared study of the performance of nanostructured TiO_2 particles for the photocatalytic oxidation of gaseous toluene, J. Catal. 202 (2) (2001) 413–420.
[29] J. Li, X. Dong, G. Zhang, W. Cui, W. Cen, Z. Wu, S.C. Lee, F. Dong, Probing ring-opening pathways for efficient photocatalytic toluene decomposition, J. Mater. Chem. A 7 (7) (2019) 3366–3374.
[30] Y. Irokawa, T. Morikawa, K. Aoki, S. Kosaka, T. Ohwaki, Y. Taga, Photodegradation of toluene over TiO_2-xNx under visible light irradiation, PCCP 8 (9) (2006) 1116, https://doi.org/10.1039/b517653k.
[31] J. Li, H. Na, X. Zeng, T. Zhu, Z. Liu, In situ DRIFTS investigation for the oxidation of toluene by ozone over Mn/HZSM-5, Ag/HZSM-5 and Mn-Ag/HZSM-5 catalysts, Appl. Surf. Sci. 311 (2014) 690–696.
[32] J. Liu, Y. Li, J. Ke, S. Wang, L. Wang, H. Xiao, Black NiO-TiO_2 nanorods for solar photocatalysis: recognition of electronic structure and reaction mechanism, Appl. Catal. B 224 (2018) 705–714.
[33] Z. Wang, P. Ma, K. Zheng, C. Wang, Y. Liu, H. Dai, C. Wang, H.-C. Hsi, J. Deng, Size effect, mutual inhibition and oxidation mechanism of the catalytic removal of a toluene and acetone mixture over TiO_2 nanosheet-supported Pt nanocatalysts, Appl. Catal. B 274 (2020), 118963.
[34] F. Zhang, X. Li, Q. Zhao, Q. Zhang, M. Tade, S. Liu, Fabrication of alpha-Fe_2O_3/In_2O_3 composite hollow microspheres: a novel hybrid photocatalyst for toluene degradation under visible light, J. Colloid Interface Sci. 457 (2015) 18–26.
[35] B. Hauchecorne, D. Terrens, S. Verbruggen, J.A. Martens, H. Van Langenhove, K. Demeestere, S. Lenaerts, Elucidating the photocatalytic degradation pathway of acetaldehyde: an FTIR in situ study under atmospheric conditions, Appl. Catal. B 106 (2011) 630–638.
[36] S. Huang, C. Zhang, H. He, Complete oxidation of o-xylene over Pd/Al_2O_3 catalyst at low temperature, Catal. Today 139 (2008) 15–23.
[37] M. Lai, J. Zhao, Q. Chen, S. Feng, Y. Bai, Y. Li, C. Wang, Photocatalytic toluene degradation over Bi-decorated TiO_2: promoted O_2 supply to catalyst's surface by metallic Bi, Catal. Today 335 (2019) 372–380.
[38] Y. Xia, Z. Wang, Y. Feng, S. Xie, Y. Liu, H. Dai, J. Deng, In situ molten salt derived iron oxide supported platinum catalyst with high catalytic performance for o-xylene elimination, Catal. Today 351 (2020) 30–36.
[39] Y. Wu, S. Yuan, R. Feng, Z. Ma, Y. Gao, S. Xing, Comparative study for low-temperature catalytic oxidation of o-xylene over doped OMS-2 catalysts: role of Ag and Cu, Molecular Catalysis 442 (2017) 164–172.
[40] M. Singh, N. Zhou, D.K. Paul, K.J. Klabunde, IR spectral evidence of aldol condensation: acetaldehyde adsorption over TiO_2 surface, J. Catal. 260 (2008) 371–379.
[41] W.C. Wu, S.J. Yang, C.H. Ho, Y.S. Lin, L.F. Liao, J.L. Lin, Crotonaldehyde formation from decomposition of ICH_2CH_2OH on powdered TiO_2, J. Phys. Chem. B 110 (2006) 9627–9631.
[42] Y. Zhang, A. Martin, H. Berndt, B. Lucke, M. Meisel, FTIR investigation of surface intermediates formed during the ammoxidation of toluene over vanadyl pyrophosphate, J. Molecular Catal. A-Chem. 118 (1997) 205–214.